The Journal of Chemical Physics ARTICLE scitation.org/journal/jcp

Effect of configuration-dependent multi-body forces on interconversion kinetics of a chiral tetramer model

Cite as: J. Chem. Phys. 155, 084105 (2021); doi: 10.1063/5.0060266
Submitted: 16 June 2021 • Accepted: 12 August 2021 •
Published Online: 30 August 2021

Nikolai D. Petsev,[1] Frank H. Stillinger,[2] and Pablo G. Debenedetti[1,a)]

AFFILIATIONS

[1] Department of Chemical and Biological Engineering, Princeton University, Princeton, New Jersey 08544, USA
[2] Department of Chemistry, Princeton University, Princeton, New Jersey 08544, USA

[a)] Author to whom correspondence should be addressed: pdebene@princeton.edu

ABSTRACT

We describe a reformulation of the four-site molecular model for chiral phenomena introduced by Latinwo *et al.* ["Molecular model for chirality phenomena," J. Chem. Phys. **145**, 154503 (2016)]. The reformulation includes an additional eight-body force that arises from an explicit configuration-dependent term in the potential energy function, resulting in a coarse-grained energy-conserving force field for molecular dynamics simulations of chirality phenomena. In this model, the coarse-grained interaction energy between two tetramers depends on their respective chiralities and is controlled by a parameter λ, where $\lambda < 0$ favors local configurations involving tetramers of opposite chirality and $\lambda > 0$ gives energetic preference to configurations involving tetramers of the same chirality. We compute the autocorrelation function for a quantitative chirality metric and demonstrate that the multi-body force modifies the interconversion kinetics such that $\lambda \neq 0$ increases the effective barrier for enantiomer inversion. Our simulations reveal that for $\lambda > 0$ and temperatures below a sharply defined threshold value, this effect is dramatic, giving rise to spontaneous chiral symmetry breaking and locking molecules into their chiral identity.

I. INTRODUCTION

Chirality is a crucial aspect of a broad spectrum of biological and chemical systems. Many organic and inorganic compounds feature non-superimposable mirror-image isomers with identical chemical formulas. Despite sharing a similar structure, these molecular mirror images can exhibit drastically different physiological behavior in the human body. For example, the right-handed (D) enantiomer of the drug thalidomide is a sedative used to treat morning sickness, whereas the left-handed (L) enantiomer is teratogenic, the presence of which resulted in a tragic wave of birth defects in the 1960s.[1] Similarly, the L-enantiomer of the rheumatoid arthritis drug penicillamine is highly toxic,[2] and the L-enantiomer of the anti-tuberculosis compound ethambutol can lead to impaired vision or blindness.[3,4] In addition to numerous pharmaceutical examples,[5] chirality has been documented to play a role in a variety of applications ranging from optoelectronic manufacturing,[4,6] chiral sensing,[6–8] catalysis,[9,10] insecticides and agrochemicals,[11,12] and membrane separations.[4,13] Enantioselective chemical production is traditionally achieved in these industries through asymmetric synthesis[10,14] or chirality-based separation,[15] since non-engineered chemical reactions typically result in ~50/50 "racemic" mixtures of left- and right-handed isomers. Therefore, it is important to develop new tools that can offer molecular-level insight and guide design principles for directing the chiral state of the system.

Beyond uses in industry, chiral symmetry breaking is a fundamental problem in our understanding of the origin of life.[16,17] Life exhibits chiral features at the molecular and mesoscopic level. The amino acids that constitute naturally occurring proteins are uniformly left-handed (as determined from the two possible arrangements of the four moieties attached to their α-carbon), and their mirror images are rarely found in nature. Similarly, RNA and DNA are composed of D-nucleotides. DNA itself is chiral, with its famous double helix structure existing in the right-handed form. RNA and DNA lose their ability to self-replicate in artificially created

heterochiral mixtures,[18] and hence, the stereochemistry of organic macromolecules is critical to their function.

Therefore, a central question is whether the emergence of this asymmetry from a presumably racemic pre-biotic world is (i) predetermined by physical laws or (ii) arising from stochastic processes. One hypothesis for scenario (i) is that parity violation in the weak nuclear force systematically propagated to larger length scales and gave preference to specific chiral forms.[19,20] Another proposed explanation is that certain inorganic materials (e.g., quartz crystals) asymmetrically adsorb L and D enantiomers, producing surface enhancement of one over the other.[21–23] Furthermore, some inorganic surfaces can catalyze the oligomerization of biomolecular building blocks,[24] which would give rise to enantiomeric excess of the resulting biologically relevant oligomer.[23] For possibility (ii), mechanisms for chiral symmetry breaking rely on a combination of autocatalysis and inhibition to amplify small random imbalances until one isomer dominates over the other and the system reaches a uniform, enantiopure state.[25,26] Recent work by Laurent *et al.* showed that complex kinetic networks composed of many chiral species can undergo spontaneous chiral symmetry breaking.[27] While theoretical work has explored possible pathways for such chiral amplification,[25,26,28–42] the Soai reaction is the only experimental demonstration of this type of process to date.[43–45] Hence, understanding the specific physical and chemical phenomena that ultimately led to the prevalence L-amino acids and D-nucleotides remains an active area of research, including through the development of new models for investigating the emergence and ubiquity of biological homochirality.

As a contribution to improved fundamental understanding of chirality-driven physical phenomena, including phase separation, we describe a simple, energy-conserving force field for molecular dynamics (MD) simulations of chiral systems. Our model, a four-site flexible molecule that can adopt interconvertible and non-superimposable mirror-image configurations, is based on the simplest naturally occurring molecule that exhibits molecular handedness, hydrogen peroxide. In future studies, this approach can be readily extended to examine different types of chiral symmetries or chain-like molecules with multiple chiral centers. In the present work, we illustrate the emergence of an eight-body force from the coarse-grained description for the chirality-dependent interactions and demonstrate that this additional contribution is required for energy conservation. The eight-body force scales linearly with the coarse-grained chiral renormalization parameter λ, which controls whether intermolecular interactions between homochiral pairs are energetically favored ($\lambda > 0$) or disfavored ($\lambda < 0$). This eight-body force modifies the kinetics of chiral interconversion, which we explore using the autocorrelation function (ACF) for a quantitative measure of single-molecule chirality. We contrast the behavior of the model with and without the eight-body contribution and investigate how the kinetics of chiral interconversion is affected for different strengths of the bias λ as well as at different temperatures.

Our results suggest that the eight-body force term always increases the energy barrier for interconversion between enantiomers, and for systems with $\lambda > 0$ below a temperature T_c, this contribution gives rise to spontaneous chiral symmetry breaking. Preliminary tests suggest what appears to be incipient phase separation below T_c, and for the purposes of our discussion, we refer to this as a critical temperature, though a detailed investigation of the model's phase separation kinetics and thermodynamics is beyond the scope of the present study. Work is currently in progress in our research group on these aspects of the model's behavior and will be reported separately. An analysis of the form of the multi-body force reveals that it deforms molecules to drive their chiral identities toward ones commensurate with the local chiral environment, and these deformations occur through changes in each molecule's bond and dihedral angles. In the present work, we illuminate the details of this molecular modeling method, its basic properties, and the effect of the multi-body forces.

The remainder of this paper is structured as follows: in Sec. II, we provide a review of the molecular chiral model, and in Sec. III, we derive the forces that arise from the gradient operator acting on the potential energy function. We find that the force between a pair of "atomic" sites belonging to two different tetramers can be decomposed into two distinct contributions: (a) the familiar Lennard-Jones (LJ) force with energy pre-factor that depends on the chirality of the two interacting tetrameric molecules and (b) an additional eight-body force (henceforth referred to as the "λ-force"), which is our focus in Sec. III. Section IV provides validation tests and demonstrates the need to account for the λ-force in order to achieve energy conservation as well as general features of the model and technical details related to its implementation. Finally, in Sec. V, we compute the autocorrelation function of a single-molecule chirality metric at different temperatures and λ values and show that a non-zero chiral bias always acts to slow down the kinetics of interconversion when the λ-force is included. We conclude our discussion in Sec. VI and offer outlook for potential future studies.

II. REVIEW OF MOLECULAR MODEL FOR CHIRALITY PHENOMENA

Latinwo *et al.*[46] introduced a coarse-grained potential energy function for molecules that exist either in a left-handed or in a right-handed configuration in order to study processes such as chiral symmetry breaking and amplification. This simple model is inspired by substances such as hydrogen peroxide and hydrogen disulfide and features molecules composed of four sites or "monomers" that lie along a three-bond backbone (Fig. 1). The shape of the tetramer molecules is determined by a set of bonded interactions that include (i) bond stretching, (ii) bond angle deformation, and (iii) dihedral

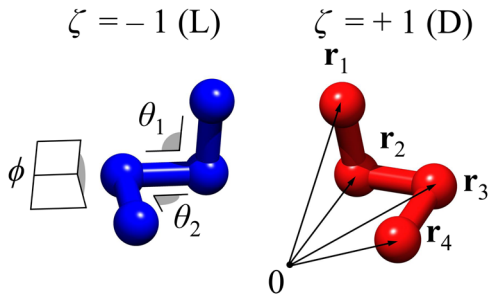

FIG. 1. Visual representation of molecules in the chiral tetramer model. Molecules are able to rotate about the dihedral angle and exist in L- (blue) or D- (red) enantiomer configurations.

TABLE I. Summary of force parameters used in our tests.

Units	k_s (kcal/mol Å^2)	k_b (kcal/mol rad^2)	k_d (kcal/mol)	b (Å)	m (g/mol)	ε_0 (kcal/mol)	σ_{tt} (Å)
Real	1000	100.0	2.775	1.18	8.5	0.1554	1.115
Reduced	8003	643.7	17.86	1.0583	1	1	1

angle rotation. The sum of these three contributions gives the total intramolecular potential energy for a single molecule,

$$\Phi^{(1)}(\{\mathbf{r}_i\}) = \sum_{i=1}^{3}\frac{k_s}{2}(r_{i,i+1}-b)^2 + \sum_{i=1}^{2}\frac{k_b}{2}\left(\theta_i-\frac{\pi}{2}\right)^2 + k_d\cos^2\phi. \quad (1)$$

Here, k_s is the force constant for the harmonic bond with equilibrium distance b, k_b is the constant for the molecular angle bending, and k_d gives the pre-factor for forces that depend on the dihedral angle. $r_{i,i+1}$ denotes the separation between the i and $i+1$ bonded monomers, θ_1 and θ_2 are the two bond angles present in the molecule, and ϕ is the dihedral angle. Note that at mechanical equilibrium, $\theta_1 = \theta_2 = \pi/2$, and $\phi = \pm\pi/2$. In our simulations, the values for the harmonic bond constant, molecular weight, and bond length b are inspired by hydrogen peroxide and written in reduced LJ units (Table I).[46–49] Note that while we use hydrogen peroxide to inform realistic choices for our parameters, this model is not intended to be an accurate representation of this substance.

For intermolecular interactions, the potential energy between monomer j from tetramer α and monomer k from tetramer γ is

$$\Phi^{(2)}_{jk}\left(\{\mathbf{r}^\alpha_j\},\{\mathbf{r}^\gamma_k\}\right) = \varepsilon_{tt}v_{LJ}\left(\frac{|\mathbf{r}^\alpha_j-\mathbf{r}^\gamma_k|}{\sigma_{tt}}\right), \quad (2)$$

where $v_{LJ} = 4\left(r_{jk}^{-12}-r_{jk}^{-6}\right)$ with $r_{jk} = |\mathbf{r}^\alpha_j-\mathbf{r}^\gamma_k|/\sigma_{tt}$. This is the standard LJ potential with interaction energy ε_{tt} and characteristic length σ_{tt}. The key feature of the chiral molecular potential is that the energy is rescaled by a renormalization factor that depends on the chiral identities of the two interacting molecules α and γ, i.e., ε_{tt} in Eq. (2) is written as[46]

$$\varepsilon_{tt} = \varepsilon_0\left[1+\lambda\zeta^\alpha\left(\{\mathbf{r}^\alpha_j\}\right)\zeta^\gamma\left(\{\mathbf{r}^\gamma_k\}\right)\right]. \quad (3)$$

Here, ζ^α and ζ^γ are measures of the chirality of molecules α and γ, respectively (defined below), and the parameter λ is a constant that controls the chiral bias in the system. ε_0 is the LJ energy of interaction between monomers in the absence of chiral bias.

The sign of λ dictates whether this favorable energy rescaling applies to homochiral or heterochiral intermolecular interactions (i.e., $\lambda < 0$ favors heterochiral interactions and racemic mixtures, and $\lambda > 0$ favors homochiral interactions and an enantiopure state). Equation (3) is a central aspect of the model, with $\lambda \neq 0$ representing a coarse-grained energetic favorability for chirality-dependent interactions between molecule pairs. This term is representative of energetic contributions and binding preferences that are not captured by the LJ potential alone. Based on their experimentally observed conglomerate (enantiopure) crystal structures, substances exhibiting behavior commensurate with a positive chiral bias include aspartic and glutamic acids,[50] while serine and histidine map to a negative chiral bias and form racemic crystals.[51] Note that the construction in Eq. (3) is mathematically similar to the interaction energy for nearest-neighbor spin pairs in the Ising model,[52,53] where the parameter λ is the coupling constant, though a critical difference in our chiral molecular model is that the energy modification in Eq. (3) couples to the molecules' internal degrees of freedom.

For the tetramer molecules in this study, the chirality measure ζ^α can be defined as

$$\zeta^\alpha = \zeta\left(\mathbf{R}^\alpha\right) = -\frac{\mathbf{r}^\alpha_{12}\cdot\left(\mathbf{r}^\alpha_{23}\times\mathbf{r}^\alpha_{34}\right)}{\left|\mathbf{r}^\alpha_{12}\right|\left|\mathbf{r}^\alpha_{23}\right|\left|\mathbf{r}^\alpha_{34}\right|}. \quad (4)$$

Note that ζ^α depends on the position vectors of all four monomers that make up the molecule, $\mathbf{R}^\alpha = \{\mathbf{r}^\alpha_1,\mathbf{r}^\alpha_2,\mathbf{r}^\alpha_3,\mathbf{r}^\alpha_4\}$, with relative vectors defined as $\mathbf{r}^\alpha_{12}\equiv\mathbf{r}^\alpha_1-\mathbf{r}^\alpha_2$. The measure Eq. (4) gives $\zeta = -1$ for L-enantiomers, $\zeta = +1$ for D-enantiomers at mechanical equilibrium, $\zeta = 0$ for transition states, and varies between these extremes as the configuration of the monomers changes with time, $\zeta\in[-1,1]$. Equation (4) is specific to the molecular geometry in this work, and different types of chiral molecules or chiral centers may require a different definition for ζ.

III. DERIVATION OF EIGHT-BODY λ-FORCE BETWEEN TETRAMER PAIRS

We now derive the forces for the chiral model, starting from the intermolecular potential defined in Sec. II. The interaction energy for two tetramers α and γ is the sum over all 16 monomer pairs,

$$\Phi^{(2)} = \sum_{j\in\alpha}\sum_{k\in\gamma}\Phi^{(2)}_{jk}. \quad (5)$$

The force acting on monomer i from tetramer α is computed from the gradient of Eq. (5),

$$\mathbf{F}^\alpha_i \equiv -\frac{\partial\Phi^{(2)}}{\partial\mathbf{r}^\alpha_i} = -\sum_j\sum_k\frac{\partial\Phi^{(2)}_{jk}}{\partial\mathbf{r}^\alpha_i}. \quad (6)$$

Substituting Eq. (2) into Eq. (6) and using $\partial v_{LJ}\left(r_{jk}\right)/\partial\mathbf{r}^\alpha_i = 0$ for $i\neq j,k$, we are left with

$$\mathbf{F}^\alpha_i = \mathbf{A}^\alpha_i + \mathbf{B}^\alpha_i, \quad (7)$$

where we have defined

$$\mathbf{A}^\alpha_i = -\sum_k\varepsilon_{tt}\frac{\partial v_{LJ}(r_{ik})}{\partial\mathbf{r}^\alpha_i} \quad (8)$$

and

$$\mathbf{B}^\alpha_i = -\left(\frac{\partial\varepsilon_{tt}}{\partial\mathbf{r}^\alpha_i}\right)\sum_j\sum_k v_{LJ}\left(r_{jk}\right). \quad (9)$$

In the above equations, $\mathbf{A}_i^\alpha$ is the LJ force on monomer i with energy of interaction $\varepsilon_{tt}(\{\mathbf{R}^\alpha\},\{\mathbf{R}^\gamma\})$ determined from the instantaneous configurations of the interacting tetramers. The decomposition into two distinct forces given by Eqs. (7)–(9) is general to any LJ-like potential with a configuration-dependent energy ε_{tt}. Strictly speaking, both $\mathbf{A}_i^\alpha$ and $\mathbf{B}_i^\alpha$ depend on the configuration of the interacting tetramers, and hence, both are eight-body forces, though we use the label "eight-body" force only in reference to the non-trivial force $\mathbf{B}_i^\alpha$.

We now focus on the λ-force contribution $\mathbf{B}_i^\alpha$ [Eq. (9)] and explicitly derive its form for the four-site chiral model. In order to determine $\mathbf{B}_i^\alpha$, we first find the gradient of the energy factor ε_{tt} evaluated at monomer i from tetramer α,

$$\frac{\partial \varepsilon_{tt}}{\partial \mathbf{r}_i^\alpha} = \lambda \zeta^\gamma \frac{\partial \zeta^\alpha}{\partial \mathbf{r}_i^\alpha}. \tag{10}$$

Equation (10) depends on which site along the tetramer backbone we consider. In the following subsections, we look at each of the four sites separately.

A. First monomer (i = 1)

Using the definition of ζ^α [Eq. (4)], and applying the gradient operator, $\nabla_{\mathbf{r}_i^\alpha} = \partial x_i^\alpha \mathbf{i}_1^\alpha + \partial y_i^\alpha \mathbf{j}_1^\alpha + \partial z_i^\alpha \mathbf{k}_1^\alpha$, we find that the gradient at the position of the first monomer ($i = 1$) is

$$\nabla_{\mathbf{r}_1^\alpha}\zeta^\alpha = -\frac{\mathbf{r}_{23}^\alpha \times \mathbf{r}_{34}^\alpha}{|\mathbf{r}_{12}^\alpha||\mathbf{r}_{23}^\alpha||\mathbf{r}_{34}^\alpha|} - \zeta^\alpha \frac{\mathbf{e}_{12}^\alpha}{|\mathbf{r}_{12}^\alpha|}. \tag{11}$$

In Eq. (11), we have defined the unit vector $\mathbf{e}_{12}^\alpha = (\mathbf{r}_1^\alpha - \mathbf{r}_2^\alpha)/|\mathbf{r}_1^\alpha - \mathbf{r}_2^\alpha|$. Using Eq. (11), the energy gradient term for the first monomer is then

$$\frac{\partial \varepsilon_{tt}}{\partial \mathbf{r}_1^\alpha} = -\lambda\zeta^\gamma \frac{(\mathbf{e}_{23}^\alpha \times \mathbf{e}_{34}^\alpha)}{|\mathbf{r}_{12}^\alpha|} \cdot \left(\mathbf{I} - \mathbf{e}_{12}^\alpha \mathbf{e}_{12}^\alpha\right). \tag{12}$$

Here, $\mathbf{I}$ denotes the identity tensor. Substituting Eq. (12) into Eq. (9) gives the λ-force acting on the first monomer, $\mathbf{B}_1^\alpha$. Note that Eq. (12) applies specifically to our current model, and choosing a different molecular geometry requires re-deriving $\partial\zeta^\alpha/\partial\mathbf{r}_i^\alpha$.

B. Second monomer (i = 2)

The gradient evaluated at the position of the second monomer is

$$\nabla_{\mathbf{r}_2^\alpha}\zeta^\alpha = -\frac{\mathbf{r}_{34}^\alpha \times \mathbf{r}_{13}^\alpha}{|\mathbf{r}_{12}^\alpha||\mathbf{r}_{23}^\alpha||\mathbf{r}_{34}^\alpha|} + \zeta^\alpha\left(\frac{\mathbf{e}_{12}^\alpha}{|\mathbf{r}_{12}^\alpha|} - \frac{\mathbf{e}_{23}^\alpha}{|\mathbf{r}_{23}^\alpha|}\right). \tag{13}$$

Rearranging Eq. (13) and substituting into Eq. (10) gives

$$\frac{\partial \varepsilon_{tt}}{\partial \mathbf{r}_2^\alpha} = \lambda\zeta^\gamma\left[\frac{(\mathbf{e}_{12}^\alpha \times \mathbf{e}_{34}^\alpha)}{|\mathbf{r}_{23}^\alpha|} \cdot \left(\mathbf{I} - \mathbf{e}_{23}^\alpha \mathbf{e}_{23}^\alpha\right) + \frac{(\mathbf{e}_{23}^\alpha \times \mathbf{e}_{34}^\alpha)}{|\mathbf{r}_{12}^\alpha|} \cdot \left(\mathbf{I} - \mathbf{e}_{12}^\alpha \mathbf{e}_{12}^\alpha\right)\right]. \tag{14}$$

Combining this expression with Eq. (9) gives $\mathbf{B}_2^\alpha$.

C. Third monomer (i = 3)

For the third monomer, we have

$$\nabla_{\mathbf{r}_3^\alpha}\zeta^\alpha = -\frac{\mathbf{r}_{12}^\alpha \times \mathbf{r}_{24}^\alpha}{|\mathbf{r}_{12}^\alpha||\mathbf{r}_{23}^\alpha||\mathbf{r}_{34}^\alpha|} + \zeta^\alpha\left(\frac{\mathbf{e}_{23}^\alpha}{|\mathbf{r}_{23}^\alpha|} - \frac{\mathbf{e}_{34}^\alpha}{|\mathbf{r}_{34}^\alpha|}\right). \tag{15}$$

Following the same procedure as above, we arrive at the following expression for the gradient of the energy factor evaluated at the third monomer,

$$\frac{\partial \varepsilon_{tt}}{\partial \mathbf{r}_3^\alpha} = -\lambda\zeta^\gamma\left[\frac{(\mathbf{e}_{12}^\alpha \times \mathbf{e}_{23}^\alpha)}{|\mathbf{r}_{34}^\alpha|} \cdot \left(\mathbf{I} - \mathbf{e}_{34}^\alpha \mathbf{e}_{34}^\alpha\right) + \frac{(\mathbf{e}_{12}^\alpha \times \mathbf{e}_{34}^\alpha)}{|\mathbf{r}_{23}^\alpha|} \cdot \left(\mathbf{I} - \mathbf{e}_{23}^\alpha \mathbf{e}_{23}^\alpha\right)\right]. \tag{16}$$

Equations (9) and (16) give $\mathbf{B}_3^\alpha$.

D. Fourth monomer (i = 4)

Finally, the gradient of the chirality measure for the last monomer is

$$\nabla_{\mathbf{r}_4^\alpha}\zeta^\alpha = -\frac{\mathbf{r}_{23}^\alpha \times \mathbf{r}_{12}^\alpha}{|\mathbf{r}_{12}^\alpha||\mathbf{r}_{23}^\alpha||\mathbf{r}_{34}^\alpha|} + \zeta^\alpha \frac{\mathbf{e}_{34}^\alpha}{|\mathbf{r}_{34}^\alpha|}. \tag{17}$$

Therefore, the gradient of the energy for $i = 4$ is

$$\frac{\partial \varepsilon_{tt}}{\partial \mathbf{r}_4^\alpha} = \lambda\zeta^\gamma \frac{(\mathbf{e}_{12}^\alpha \times \mathbf{e}_{23}^\alpha)}{|\mathbf{r}_{34}^\alpha|} \cdot \left(\mathbf{I} - \mathbf{e}_{34}^\alpha \mathbf{e}_{34}^\alpha\right). \tag{18}$$

Combining Eqs. (9) and (18) gives $\mathbf{B}_4^\alpha$.

Note that the total force acting on the tetramer due to the λ-force contributions is zero. To illustrate this, we sum all four forces for molecule α,

$$\begin{aligned}\mathbf{B}^\alpha &= \mathbf{B}_1^\alpha + \mathbf{B}_2^\alpha + \mathbf{B}_3^\alpha + \mathbf{B}_4^\alpha \\ &= -\left(\frac{\partial \varepsilon_{tt}}{\partial \mathbf{r}_1^\alpha} + \frac{\partial \varepsilon_{tt}}{\partial \mathbf{r}_2^\alpha} + \frac{\partial \varepsilon_{tt}}{\partial \mathbf{r}_3^\alpha} + \frac{\partial \varepsilon_{tt}}{\partial \mathbf{r}_4^\alpha}\right)\sum_j\sum_k v_{LJ}(r_{jk}).\end{aligned} \tag{19}$$

From Eqs. (12), (14), (16), and (18), we find that

$$\frac{\partial \varepsilon_{tt}}{\partial \mathbf{r}_1^\alpha} + \frac{\partial \varepsilon_{tt}}{\partial \mathbf{r}_2^\alpha} + \frac{\partial \varepsilon_{tt}}{\partial \mathbf{r}_3^\alpha} + \frac{\partial \varepsilon_{tt}}{\partial \mathbf{r}_4^\alpha} = 0. \tag{20}$$

Therefore, the net force between tetramer pairs due to the λ-force $\mathbf{B}^\alpha$ vanishes, and only the "standard" Lennard-Jones contribution $\mathbf{A}^\alpha$ is relevant to the center-of-mass force acting between tetramer pairs. In other words, the eight-body forces cause molecular deformation, but not center-of-mass translation.

The λ-force between two tetramers tends to deform the interacting molecules and modify each molecule's chiral identity through its bond and dihedral angles, and therefore, this force can be re-expressed as deformation forces acting on θ_1^α, θ_2^α, and ϕ^α. In other words, there is a distinct λ-force contribution $\mathbf{B}_{ij}^\alpha$ for every bond and dihedral angle in molecule α, *i.e.*, $|\mathbf{B}_{12}^\alpha| \propto \sin\theta_2^\alpha$, $|\mathbf{B}_{23}^\alpha| \propto \sin\phi^\alpha$, and $|\mathbf{B}_{34}| \propto \sin\theta_1^\alpha$. The proportionality with respect to the sine of bond and dihedral angles comes from the unit vector cross products in Eqs. (21)–(23). The fact that the λ-forces can be rewritten in this fashion is seen by inspection of the final form of $\mathbf{B}_1^\alpha$, $\mathbf{B}_2^\alpha$, $\mathbf{B}_3^\alpha$, and $\mathbf{B}_4^\alpha$.

We now rewrite the multi-body λ-forces using this decomposition, which is more elegant and convenient to implement numerically, gives additional physical intuition for the nature of the λ-forces, and illustrates why the net λ-force on each molecule is zero. First, we consider how the $\alpha - \gamma$ tetramer pair multi-body λ-force deforms tetramer α by acting on its bond angle θ_2^α in a way that gives rise to an effective interaction between the 1–2 monomer pair,

$$\mathbf{B}_{12}^{\alpha} = \lambda\zeta^{\gamma}\frac{(\mathbf{e}_{23}^{\alpha}\times\mathbf{e}_{34}^{\alpha})}{|\mathbf{r}_{12}^{\alpha}|}\cdot\left(\mathbf{I}-\mathbf{e}_{12}^{\alpha}\mathbf{e}_{12}^{\alpha}\right)\sum_{j}\sum_{k}v_{LJ}(r_{jk}). \tag{21}$$

Equation (21) is the force on monomer 1, and the force on monomer 2 (which is bonded to monomer 1) is symmetric, $\mathbf{B}_{21}^{\alpha} = -\mathbf{B}_{12}^{\alpha}$. While this formulation of the forces superficially appears pairwise, the λ-force is still fundamentally a multi-body interaction that depends on the full tetramer configurations. To understand why the multi-body force can be decomposed into these kinds of interactions, consider that the force between monomers 1 and 2 in Eq. (21) is proportional to the cross product of the normalized bond vectors $\mathbf{e}_{23}^{\alpha}$ and $\mathbf{e}_{34}^{\alpha}$, which directly relates to molecule α's bond angle θ_2^α, i.e., $|\mathbf{B}_{12}^{\alpha}| \propto \sin\theta_2^\alpha$. Hence, the multi-body λ-force affects molecule α's chiral identity by acting on the bond angle θ_2^α through the force $\mathbf{B}_{12}^{\alpha}$ between monomers 1 and 2.

The λ-force acting on the dihedral angle ϕ^α results in the symmetric force between monomers 2 and 3, with force acting on monomer 2 given by

$$\mathbf{B}_{23}^{\alpha} = -\lambda\zeta^{\gamma}\frac{(\mathbf{e}_{12}^{\alpha}\times\mathbf{e}_{34}^{\alpha})}{|\mathbf{r}_{23}^{\alpha}|}\cdot\left(\mathbf{I}-\mathbf{e}_{23}^{\alpha}\mathbf{e}_{23}^{\alpha}\right)\sum_{j}\sum_{k}v_{LJ}(r_{jk}). \tag{22}$$

Once again, the force on monomer 3 for this pair is equal and opposite, $\mathbf{B}_{32}^{\alpha} = -\mathbf{B}_{23}^{\alpha}$.

Finally, the λ-force deformations of the bond angle θ_1^α result in a symmetric interaction between monomers 3 and 4,

$$\mathbf{B}_{34}^{\alpha} = \lambda\zeta^{\gamma}\frac{(\mathbf{e}_{12}^{\alpha}\times\mathbf{e}_{23}^{\alpha})}{|\mathbf{r}_{34}^{\alpha}|}\cdot\left(\mathbf{I}-\mathbf{e}_{34}^{\alpha}\mathbf{e}_{34}^{\alpha}\right)\sum_{j}\sum_{k}v_{LJ}(r_{jk}). \tag{23}$$

As before, we have $\mathbf{B}_{43}^{\alpha} = -\mathbf{B}_{34}^{\alpha}$. Equations (21)–(23) then summarize the λ-forces, which are the central focus of this paper. Adding Eqs. (21)–(23) over bonded monomer pairs within a single tetramer results in the same λ-force for each monomer as in Eq. (9). The full intermolecular forces are given by the sum of the λ-forces [Eqs. (21)–(23)] and LJ-like forces [Eq. (8)]. Note that this non-trivial interaction does not depend on which end of the molecule we count labels from, and performing the symmetric exchange of indices $i = 1 \to 4$, $i = 2 \to 3$, $i = 3 \to 2$, and $i = 4 \to 1$ gives identical force expressions.

To gain additional physical intuition for the λ-forces, we examine their form more closely. As discussed above, Eqs. (21)–(23) are proportional to cross products whose magnitudes relate to the angles between the bond vectors in molecule α, i.e., $|\mathbf{B}_{12}^{\alpha}| \propto \sin\theta_2^\alpha$, $|\mathbf{B}_{23}^{\alpha}| \propto \sin\phi^\alpha$, and $|\mathbf{B}_{34}| \propto \sin\theta_1^\alpha$. Therefore, these forces vanish for states far from mechanical equilibrium, where $\theta_1^\alpha = \theta_2^\alpha = \pi$, as well as for the transition states $\phi^\alpha = \pm\pi$ and $\phi^\alpha = 0$. They are also zero for $\theta_1^\alpha = \theta_2^\alpha = \phi^\alpha = \pm\pi/2$, though in this case due to cancellation of terms [e.g., the terms on the right-hand side of Eq. (11) are equal in magnitude but opposite in sign]. The λ-forces are non-zero for all configurations in between these cases, and their effect is to oppose interconversion when $\lambda < 0$ and the two interacting tetramers have different chiral identities (i.e., an L-tetramer and a D-tetramer) and to oppose interconversion when $\lambda > 0$ and the two interacting tetramers have the same chiral identity (i.e., two L-tetramers or two D-tetramers). In other words, this additional force resists inversion away from the chiral state imposed on the molecule's local environment by the renormalization term λ. For initially racemic systems below some critical temperature $T < T_c$, the λ-force drives spontaneous chiral symmetry breaking. This is demonstrated in Sec. V, where we study the effect of the λ-force for different values of the chiral bias λ and show that it always gives slower inversion kinetics for molecules at equilibrium relative to the case without this force. Note that criticality and the thermodynamics and kinetics of phase separation for this model are beyond the scope of the current study and will be reported in future work.

IV. VALIDATION

We have implemented the chiral tetramer model into the LAMMPS package[54,55] and now validate that our approach conserves energy by performing MD simulations of 1000 chiral molecules (4000 monomers) in the microcanonical ensemble. We choose values for the intermolecular interaction and intramolecular bond constants in reduced LJ units as summarized in Table I.[46–49] These model parameters are used for all tests in this work unless otherwise noted. The validation is performed with $\lambda = 0.5$ for the chiral renormalization term, since $\lambda = 0.0$ gives the trivial case for a LJ chain. The 1000 tetramers are initialized in a box with dimensions $16.8 \times 16.8 \times 16.8$ and periodic boundaries in the x-, y-, and z-directions, corresponding to a molecular density of $\rho = 0.21$. We choose a time step $\Delta t = 0.001$ and equilibrate for 1×10^8 steps using a Nosé–Hoover thermostat with $T = 4.0$. Following the initialization, we perform a production run at constant NVE for another 1×10^8 time steps. The tests described here use eight processors and feature a large potential cutoff $r_c = 4.0$ to ensure that molecules have sufficient neighbors to capture the eight-body effect. Our NVE tests (summarized below) suggest that r_c values smaller than 4.0 give inadequate energy conservation for $\lambda = 0.5$ (the maximum λ value considered in this work), and a larger cutoff is required.

Before discussing the energy conservation properties of this model, we first illustrate the effect of the chiral renormalization term λ, which is a central feature of this model and biases systems toward enantiopure equilibrium states. The visualizations in Fig. 2 are obtained from trajectories in the NVT ensemble with $\rho = 0.21$ and $T = 4.0$. Here, each sphere represents the center of mass of a tetramer, with color determined by the chiral identity of the molecule (e.g., blue spheres are L-enantiomers, and red spheres are isomers in the D configuration). Figure 2(a) is a visual representation of the equilibrium state for a fluid with renormalization term $\lambda = 0.5$. As expected, the positive chiral bias favors homochiral interactions, giving a predominantly L-enantiomer fluid. Note that a small number of D-enantiomers are present (red spheres), as expected for a system at finite temperature. Such fluctuations in ζ away from the equilibrium value become vanishingly rare at lower

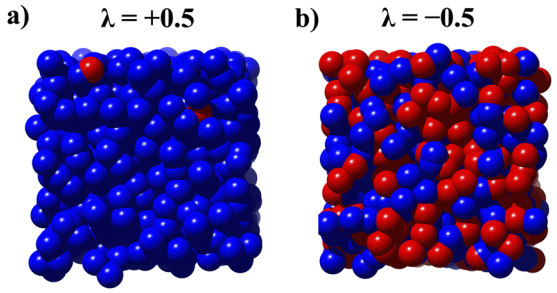

FIG. 2. (a) Visualization of the system for $\lambda = 0.5$ and $T = 4.0$, where the positive λ value favors a globally enantiopure state. Each sphere represents a tetramer molecule and is located at its center of mass, with color coding based on whether the tetramer is in a L (blue) or D (red) configuration. (b) Visualization for $\lambda = -0.5$ at the same temperature. Here, the negative chiral bias gives rise to a racemic mixture.

temperatures. Conversely, the equivalent case with a negative chiral bias $\lambda = -0.5$ (i.e., favoring heterochiral interactions) is illustrated in Fig. 2(b), giving a racemic mixture of L- and D-enantiomers.

The kinetic, potential, and total system energies for the NVE validation tests are shown in Fig. 3(a). In order to display these three energies compactly, we center them at zero and plot the difference relative to the energy at the start of the production run. As illustrated by the black curve in Fig. 3(a), energy is conserved to good accuracy over the course of the production run, with a mean of $\langle E_{tot} \rangle = 15\,502.99$ and relative root-mean-square error in the total energy $\langle \Delta E^2 \rangle^{1/2} / \langle E \rangle = 3.1 \times 10^{-5}$.

To illuminate the effect of the eight-body λ-force derived in Sec. III, we also perform tests with this force turned off. In other words, we initialize and run a set of separate simulations where the intermolecular forces are given by Eq. (8), and we do not include the λ-contribution $\mathbf{B}_i^\alpha$. Given that $\mathbf{B}_i^\alpha$ arises from the gradient of the potential energy function, these additional tests do not feature a conservative force field. Latinwo *et al.* incorrectly overlooked the λ-force contribution and studied the "unbalanced" force model in detail in Ref. 46. However, the unbalanced force formulation still represents a useful model, and it is interpreted as a steady-state, nonequilibrium system with physical behavior similar to the reactive binary mixture described by Glotzer *et al.*[56,57] In other words, when the λ-force is not included, the resulting force imbalance acts as a racemizing force that sustains demixing and gives kinetically arrested liquid–liquid phase separation. We find that when we use the unbalanced force formulation in the microcanonical ensemble, the system exhibits upward drift in the energy with time [red curve, Fig. 3(b)], as compared to the balanced force model [black curve, Fig. 3(b)], until the simulation eventually crashes near $t \approx 300$. For the NVT tests in Sec. V, the unbalanced force model works stably since the thermostat acts as an energy sink that dissipates the energy drift. We explore the difference in interconversion kinetics between the balanced and unbalanced force models in Sec. V. Further discussion on the unbalanced force model, its phase behavior, and how its physical properties differ from the balanced force model is the subject of ongoing work and will be reported in a future publication.

The kinetic behavior for a selected tetramer is illustrated in Fig. 3(c), which gives its chiral identity as measured by ζ [Eq. (4)] vs time. Over the course of the simulation, the molecule flips between the L ($\zeta < 0$) and D ($\zeta > 0$) states. The magenta curve gives the chiral identity for a tetramer in a fluid with molecules having a dihedral force constant $k_d = 17.86$, and the cyan curve corresponds to the case when the bond constant is an order of magnitude smaller. This clearly shows that lowering the energy barrier for interconversion increases the frequency for excursions away from the average

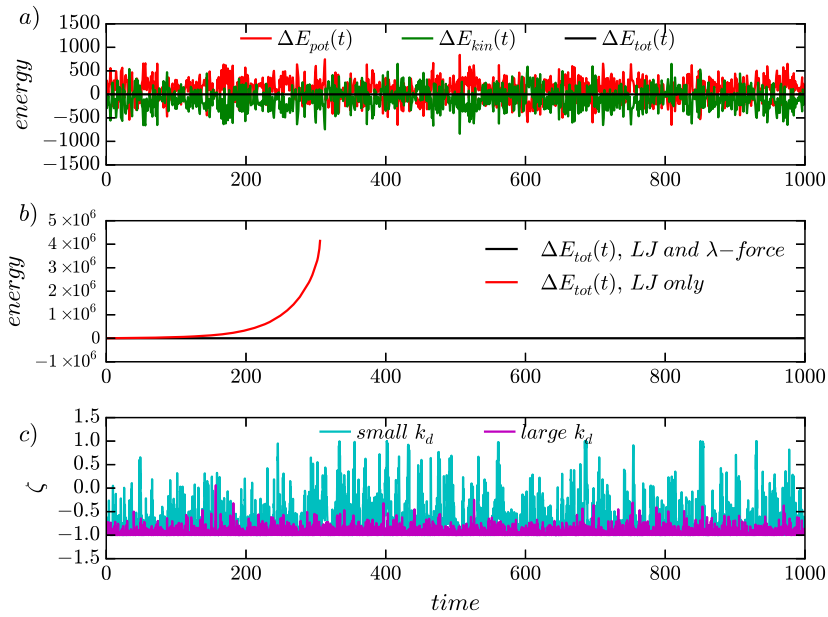

FIG. 3. (a) System potential (red curve), kinetic (green curve), and total energies (black curve) as a function of time for NVE simulation of a tetramer fluid with $\lambda = 0.5$, $\rho = 0.21$, and average temperature $\langle T \rangle = 4.0$. Note that energies are not absolute and are centered at zero for clarity. (b) Total energy vs time for the balanced (black curve) and unbalanced (red curve) force tetramer models. (c) Chiral identity ζ of a single tetramer vs time. The two colors denote identical simulation conditions with different dihedral interaction force constants to illustrate how changing the energy barrier for interconversion affects the frequency for switching between L and D forms. An excess of L enantiomers in the initial configuration biases the system toward $\langle \zeta \rangle = -1$ for both k_d cases.

system value. For both choices of k_d, the system globally adopts an enantiopure state with preferred chiral identity $\langle\zeta(t)\rangle \approx -1.0$. Note that whether the system equilibrates to $\langle\zeta(t)\rangle \approx -1.0$ or $\langle\zeta(t)\rangle \approx +1.0$ is arbitrary, and both are equally probable assuming an initial 50/50 mixture of L and D enantiomers. In our work, the initial pre-equilibration configuration features a 1.6% excess of L-enantiomers due to the preparation procedure, which is why the system exhibits preference for the $\langle\zeta(t)\rangle \approx -1.0$ equilibrium state when $\lambda > 0$. Figure 3(c) shows that multiple times throughout the production run, the selected molecule flips its chirality away from this preferred chiral state due to thermal fluctuations, and these random inversions are rapidly dissipated. At temperatures below a critical threshold $T < T_c$, tetramer chiral identities are strongly locked-in, with fewer (or even zero) flips due to thermal kicks, and smaller fluctuations in the chiral measure ζ. This behavior is similar to spontaneous magnetization below the critical point in the Ising model, where broken symmetry persists despite fluctuations in spins. Section V explores this behavior in detail and highlights the crucial contribution of the λ-force to capture spontaneous chiral symmetry breaking.

V. EIGHT-BODY EFFECT ON TETRAMER INTERCONVERSION KINETICS

To study the inversion kinetics of the tetramer system, we calculate the autocorrelation function (ACF) for the chirality measure ζ,

$$C_\zeta(\Delta t) = \frac{\langle\zeta(t_0+\Delta t)\cdot\zeta(t_0)\rangle}{\langle\zeta(t_0)\cdot\zeta(t_0)\rangle}. \tag{24}$$

Here, the brackets denote an ensemble average over all of the molecules in the system at a given time. Additionally, we compute an average over multiple independent trajectories to remove statistical noise from a set of NVT simulations with 1000 tetramers at a reduced density $\rho = 0.21$. This density was selected to ensure our system is in the liquid state and to avoid the formation of a vapor phase. We consider λ values of −0.5, 0.0, and 0.5 and perform tests with and without the eight-body λ-force in order to illustrate its effect, which is pronounced at lower temperatures $T < T_c$. Note that the tests without the λ-force do not represent a conservative force field (as described in Sec. IV), and we include these unbalanced force results to illustrate the strong effect of the λ-forces. In these cases, the energy drift due to the absence of the λ-forces is quenched by application of the thermostat.

Figure 4(a) shows the ACFs for the molecule chiral identities at $T = 4.0$. The black dashed curve is the result with no chiral bias ($\lambda = 0$). This represents a simple LJ chain with the bond and dihedral angle parameters specified in Table I. The green curve gives the $\lambda = +0.5$ case that favors homochiral interactions, and the red curve is the $\lambda = -0.5$ case that favors a locally racemic environment. The curves for the ACFs from runs without the λ-force contribution are nearly identical to the $\lambda = 0$ case (dashed black curve) and are omitted for clarity. For the purposes of our discussion, the dashed black curve also represents the $\lambda = +0.5$ and −0.5 cases when the λ-force is not included, and the solid curves give the corresponding ACFs for identical simulation conditions, but also including the λ-force. At $T = 4.0$, the system is enantiopure with the choice $\lambda = 0.5$, while for the $\lambda = 0.0$ and $\lambda = -0.5$ tests, the system is racemic. Chiral configurations without the eight-body force decorrelate at a rate comparable to that occurring without chiral bias (black dashed curve), while including the λ-force with $\lambda \neq 0$ results in slower kinetics relative to the $\lambda = 0$ case (solid red and green curves). Importantly, when $\lambda > 0$ and the λ-force is included, chiral configurations at $T = 4.0$ persist over very long times, giving an approximately constant ACF value over the times considered. Hence, the effect of the λ-force is to drive spontaneous chiral symmetry breaking and lock molecules into a configuration aligned with the energetically favorable chiral state. This "locked-in" effect disappears at higher temperatures [e.g., $T = 6.0$, Fig. 4(b)], where the system is racemic for both $\lambda = +0.5$ and −0.5. The λ-force is therefore a crucial component of this model and drives behavior that appears analogous to spontaneous magnetization below the critical temperature in the Ising model, with the sign of the coupling constant (in our case, the parameter λ) determining whether we bias toward enantiopure or racemic systems.

Why does a positive value of λ give a larger energy barrier for inversion than a negative one? First consider an enantiopure

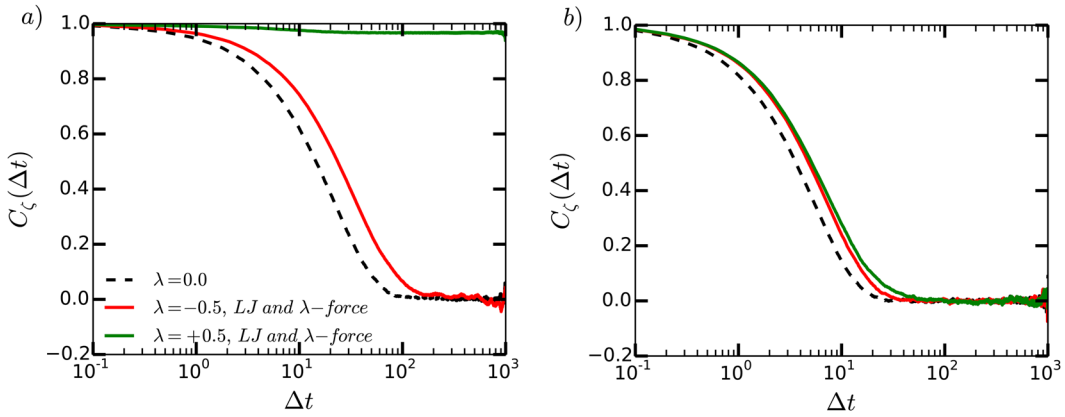

FIG. 4. (a) Autocorrelation functions for the chirality measure ζ at $T = 4.0$. The dashed curve is the ACF for $\lambda = 0.0$. ACFs for the case without the λ-force are omitted for clarity and are nearly identical to the $\lambda = 0.0$ case. Solid curves are ACFs with the λ-force. (b) Same as in (a), but for $T = 6.0$.

fluid with $\lambda > 0$, where all molecules are in the L-configuration. If we focus on a local region in the fluid containing six molecules and flip molecule α into the D configuration, where α is one of the six selected molecules, all five remaining neighbors will exert λ-forces that act to reverse molecule α's flip. Therefore, flipping the chiral identity of molecule α from L to D results in five energetically unfavorable interactions for the enantiopure case. Now suppose we have a racemic fluid with $\lambda < 0$, and we instead examine a local region where we have three L-enantiomers and three D-enantiomers. If we flip the identity of L-enantiomer α so that it exists in the D-configuration instead, molecule α now experiences more favorable energetic interactions with the two remaining L-enantiomers, and less favorable interactions with the three other D-enantiomers. Therefore, we again have more energetically unfavorable interactions (3) than favorable ones (2), though this mix of more and less favorable interactions results in a smaller energy barrier for chiral interconversion relative to the enantiopure scenario. Hence, $\lambda \neq 0$ will always increase the energy barrier for interconversion, and this effect is more pronounced for positive chiral bias $\lambda > 0$.

We conclude our examination of the chiral tetramer model by studying the temperature effect on chiral interconversion for the $\lambda \neq 0$ cases. To this end, we perform a set of tests across a number of temperatures and then fit an exponential with the form $A\ \exp(-t/\langle t_{inv}\rangle)$ to the ACFs in order to extract an average tetramer inversion time $\langle t_{inv}\rangle$. Figure 5 shows $\langle t_{inv}\rangle$ as a function of temperature for $\lambda = -0.5$, 0.0, and +0.2. Figure 5 illustrates how $\lambda \neq 0$ always results in slower kinetics, with both positive (green curve) and negative (red curve) chiral biases giving larger times than the bias-free case (black dashed curve). As expected, the time scale for chiral interconversion decreases monotonically with temperature. For $\lambda = -0.5$, a higher temperature is required to give comparable interconversion times when compared to the $\lambda = 0.0$ case, a reflection of how the λ-forces increase the energy barrier for chiral identity inversion. This effect is modest for temperatures above T_c (Fig. 5) and substantial for $\lambda > 0$ and $T < T_c$, in which case we were unable to extract interconversion times since enantiopure systems exhibit locked-in molecules with an approximately constant ACF [see Fig. 4(a), green curve], and hence, an exponential fit was not possible. Therefore, the curve for $\lambda = 0.2$ in Fig. 5 does not extend below $T = 4.0$ (denoted by the circle marker) since spontaneous chiral symmetry breaking was observed below this temperature.

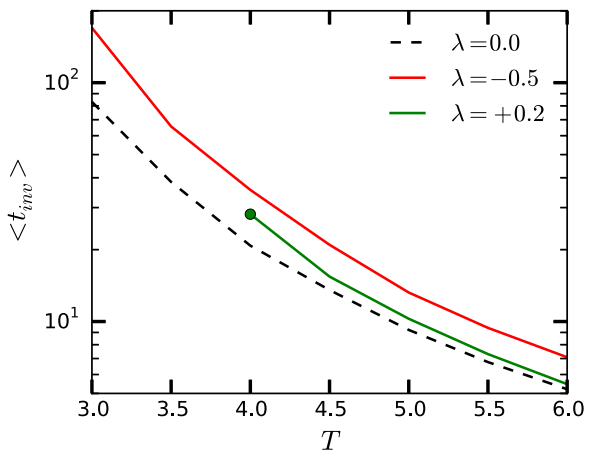

FIG. 5. Average tetramer inversion time vs temperature. Note that all tests with $\lambda \neq 0$ exhibit a modest increase in the inversion time and hence slower kinetics relative to the $\lambda = 0$ case. This effect becomes dramatic for enantiopure systems, and the circle marker denotes the lowest temperature where it was possible to extract an inversion time for the $\lambda > 0$ case.

VI. CONCLUSION

In this work, we described an energy-conserving force field for studying chirality phenomena inspired by simple substances, such as hydrogen peroxide and hydrogen disulfide. The model is composed of Lennard-Jones chains with four monomer units. Bond angle and dihedral angle force constants are chosen such that the molecules can exist in either a left-handed or a right-handed configuration, and energetic preference for racemic or enantiopure fluids is introduced through a coarse-grained parameter λ. From this molecular potential, we derived an eight-body λ-force that emerges, in addition to the Lennard-Jones-like intermolecular forces in the system, due to the gradient operator acting on the chiral renormalization term. To illustrate the influence of this non-trivial force, we calculated autocorrelation functions for a single-molecule chirality measure and demonstrated that the λ-force acts to oppose chiral interconversion at equilibrium, giving rise to spontaneous chiral symmetry breaking below a sharply defined temperature $T < T_c$. Finally, we quantified the influence of temperature on the tetramer interconversion kinetics when $\lambda \neq 0$ and showed that the λ-force effect is most significant for positive chiral bias and below T_c.

The model offers a simplified and coarse-grained strategy for investigating phenomena such as chiral amplification and the nucleation and growth of enantiopure phases. Our approach can be generalized in future work to include chiral centers with different geometries or bond numbers, as well as longer Lennard-Jones chains with one or more chiral centers, extending our coarse-grained modeling approach to capture a broader set of molecules where additional energetic contributions (e.g., hydrogen bonding) can play a role in influencing chirality. Generalizing our model to larger molecules opens a pathway for mapping to a much broader spectrum of chiral substances, since the possibility for chiral features in a molecule increases with the number of atoms that make up the molecule.[27] Another interesting potential direction is to investigate solid phase behavior of the tetrameric model presented here, since exploring the conditions that give rise to conglomerate and racemate crystal structures is relevant to enantioselective chemical production applications. Previous attempts by Latinwo *et al.* to crystallize the unbalanced force chiral tetramer model using direct MD simulations were unsuccessful,[46] and crystallization in general is difficult to study using MD.[58] As a first-pass at resolving this issue, Latinwo *et al.* obtained inherent structures from isochoric MD simulations of a two-tetramer system.[46] Building on this previous study, one intriguing possibility is to explore alternate strategies (e.g., genetic algorithms) to find the ground state configurations of the chiral molecular model and use those optimized crystal structures as starting points for our solid-phase MD tests to explore the solid-phase structures formed by the balanced force chiral tetramer model. This type of study would offer a foundation for finding the stable lattices

for the tetrameric molecules for different choices of the chiral renormalization term, and investigate under what conditions (e.g., temperature and pressure) they form conglomerate crystals vs racemate ones.

ACKNOWLEDGMENTS

The authors are grateful to Sergey Buldyrev for suggesting the presence of a configuration-dependent energy term as a possible source of non-conservative forces in the original model formulation and to Yiming Wang and Betul Uralcan for useful discussions regarding this work. The simulations presented in this article were performed on computational resources managed and supported by Princeton Research Computing, a consortium of groups including the Princeton Institute for Computational Science and Engineering (PICSciE) and the Office of Information Technology's High Performance Computing Center and Visualization Laboratory at Princeton University. Molecular visualization was performed with the UCSF Chimera package. Chimera is developed by the Resource for Biocomputing, Visualization, and Informatics at the University of California, San Francisco (supported by NIGMS Grant No. P41-GM103311). P.G.D. gratefully acknowledges support from the National Science Foundation (Grant No. CHE-1856704).

DATA AVAILABILITY

The source code and input files for the chiral tetramer molecular model presented in this study are openly available for download in the Princeton DataSpace repository at https://doi.org/10.34770/ybs9-5t93.[55]

REFERENCES

[1] S. K. Teo, W. A. Colburn, W. G. Tracewell, K. A. Kook, D. I. Stirling, M. S. Jaworsky, M. A. Scheffler, S. D. Thomas, and O. L. Laskin, Clin. Pharmacokinet. **43**, 311 (2004).
[2] W. F. Kean, H. E. Howard-Lock, and C. J. L. Lock, Lancet **338**, 1565 (1991).
[3] N. Chhabra, M. L. Aseri, and D. Padmanabhan, Int. J. Appl. Basic Med. Res. **3**, 16 (2013).
[4] W. A. Nugent, T. V. RajanBabu, and M. J. Burk, Science **259**, 479 (1993).
[5] *Chiral Drugs: Chemistry and Biological Action*, 1st ed. edited by G.-Q. Lin, Q.-D. You, and J.-F. Cheng (Wiley, Hoboken, NJ, 2011).
[6] J. Govan and Y. K. Gun'ko, Nanoscience **3**, 1–30 (2016).
[7] K. Ariga, G. J. Richards, S. Ishihara, H. Izawa, and J. P. Hill, Sensors **10**, 6796 (2010).
[8] M. Hentschel, M. Schäferling, X. Duan, H. Giessen, and N. Liu, Sci. Adv. **3**, e1602735 (2017).
[9] T. Mallat, E. Orglmeister, and A. Baiker, Chem. Rev. **107**, 4863 (2007).
[10] C.-D. Wu, A. Hu, L. Zhang, and W. Lin, J. Am. Chem. Soc. **127**, 8940 (2005).
[11] W. Liu, J. Gan, D. Schlenk, and W. A. Jury, Proc. Natl. Acad. Sci. U. S. A. **102**, 701 (2005).
[12] A. R. Aguiar, E. S. Alvarenga, E. M. Silva, E. S. Farias, and M. C. Picanço, Pest Manage. Sci. **75**, 1689 (2019).
[13] R. Xie, L.-Y. Chu, and J.-G. Deng, Chem. Soc. Rev. **37**, 1243 (2008).
[14] R. Noyori, *Asymmetric Catalysis in Organic Synthesis* (Wiley, 1993).
[15] A. M. Stalcup, Annu. Rev. Anal. Chem. **3**, 341 (2010).
[16] M. Yus and A. Guijarro, *The Origin of Chirality in the Molecules of Life: A Revision from Awareness to the Current Theories and Perspectives of this Unsolved Problem*, 1st ed. (Royal Society of Chemistry, Cambridge, 2009).
[17] W. J. Lough and I. W. Wainer, *Chirality in Natural and Applied Science* (Wiley-Blackwell, Oxford, 2006).
[18] K. Hoehlig, L. Bethge, and S. Klussmann, PLoS One **10**, e0115328 (2015).
[19] D. K. Kondepudi and G. W. Nelson, Physica A **125**, 465 (1984).
[20] D. K. Kondepudi and G. W. Nelson, Nature **314**, 438 (1985).
[21] L. Keszthelyi, Q. Rev. Biophys. **28**, 473 (1995).
[22] W. A. Bonner, Origins Life Evol. Biospheres **21**, 59 (1991).
[23] R. M. Hazen and D. S. Sholl, Nat. Mater. **2**, 367 (2003).
[24] J. P. Ferris and G. Ertem, Science **257**, 1387 (1992).
[25] F. C. Frank, Biochim. Biophys. Acta **11**, 459 (1953).
[26] D. G. Blackmond, Cold Spring Harbor Perspect. Biol. **11**, a032540 (2019).
[27] G. Laurent, D. Lacoste, and P. Gaspard, Proc. Natl. Acad. Sci. U. S. A. **118**, e2012741118 (2021).
[28] D. G. Blackmond, C. R. McMillan, S. Ramdeehul, A. Schorm, and J. M. Brown, J. Am. Chem. Soc. **123**, 10103 (2001).
[29] H. W. Hatch, F. H. Stillinger, and P. G. Debenedetti, J. Chem. Phys. **133**, 224502 (2010).
[30] D. G. Blackmond, Proc. Natl. Acad. Sci. U. S. A. **101**, 5732 (2004).
[31] F. Jafarpour, T. Biancalani, and N. Goldenfeld, Phys. Rev. E **95**, 032407 (2017).
[32] D. G. Blackmond, Chem. Rev. **120**, 4831 (2020).
[33] F. Jafarpour, T. Biancalani, and N. Goldenfeld, Phys. Rev. Lett. **115**, 158101 (2015).
[34] D. K. Kondepudi and G. W. Nelson, Phys. Rev. Lett. **50**, 1023 (1983).
[35] R. Plasson, D. K. Kondepudi, H. Bersini, A. Commeyras, and K. Asakura, Chirality **19**, 589 (2007).
[36] D. K. Kondepudi and K. Asakura, Acc. Chem. Res. **34**, 946 (2001).
[37] J. A. D. Wattis and P. V. Coveney, Origins Life Evol. Biospheres **35**, 243 (2005).
[38] R. Kafri, O. Markovitch, and D. Lancet, Biol. Direct **5**, 38 (2010).
[39] Y. Saito and H. Hyuga, Rev. Mod. Phys. **85**, 603 (2013).
[40] M. Stich, J. M. Ribó, D. G. Blackmond, and D. Hochberg, J. Chem. Phys. **145**, 074111 (2016).
[41] D. Hochberg, R. D. Bourdon García, J. A. Ágreda Bastidas, and J. M. Ribó, Phys. Chem. Chem. Phys. **19**, 17618 (2017).
[42] R. Plasson, H. Bersini, and A. Commeyras, Proc. Natl. Acad. Sci. U. S. A. **101**, 16733 (2004).
[43] K. Soai, T. Shibata, H. Morioka, and K. Choji, Nature **378**, 767 (1995).
[44] T. Shibata, K. Choji, T. Hayase, Y. Aizu, and K. Soai, Chem. Commun. **1996**, 1235.
[45] T. Shibata, H. Morioka, T. Hayase, K. Choji, and K. Soai, J. Am. Chem. Soc. **118**, 471 (1996).
[46] F. Latinwo, F. H. Stillinger, and P. G. Debenedetti, J. Chem. Phys. **145**, 154503 (2016).
[47] R. L. Redington, W. B. Olson, and P. C. Cross, J. Chem. Phys. **36**, 1311 (1962).
[48] R. H. Hunt, R. A. Leacock, C. W. Peters, and K. T. Hecht, J. Chem. Phys. **42**, 1931 (1965).
[49] R. I. Cukier and S. A. Seibold, J. Phys. Chem. B **106**, 12031 (2002).
[50] C. Viedma, Origins Life Evol. Biospheres **31**, 501 (2001).
[51] H. N. Bordallo, B. A. Kolesov, E. V. Boldyreva, and F. Juranyi, J. Am. Chem. Soc. **129**, 10984 (2007).
[52] E. Ising, Z. Phys. **31**, 253 (1925).
[53] B. M. McCoy and T. T. Wu, *The Two-Dimensional Ising Model*, 2nd ed. (Courier Corporation, 2014).
[54] S. Plimpton, J. Comput. Phys. **117**, 1 (1995).
[55] N. D. Petsev, F. H. Stillinger, and P. G. Debenedetti, Chiral Tetramer Molecular Model Source Code, http://arks.princeton.edu/ark:/88435/dsp01z890rx36m, Princeton DataSpace, 2021.
[56] S. C. Glotzer, D. Stauffer, and N. Jan, Phys. Rev. Lett. **72**, 4109 (1994).
[57] S. C. Glotzer, E. A. Di Marzio, and M. Muthukumar, Phys. Rev. Lett. **74**, 2034 (1995).
[58] R. Martoňák, A. Laio, and M. Parrinello, Phys. Rev. Lett. **90**, 075503 (2003).